

# Single- and Double-Sided Marchenko Imaging Conditions in Acoustic Media

Joost van der Neut<sup>1</sup>, Joeri Brackenhoff, Myrna Staring<sup>2</sup>, Lele Zhang<sup>3</sup>, Sjoerd de Ridder<sup>4</sup>, Evert Slob<sup>5</sup>, and Kees Wapenaar<sup>6</sup>

**Abstract**—In acoustic reflector imaging, we deploy sources and receivers outside a volume to collect a multisource, multioffset reflection response in order to retrieve the internal reflectivity of that volume. It has been shown that Green’s functions inside the volume can be retrieved by single-sided wavefield focusing of the acquired reflection data, using so-called focusing functions, which can be computed by solving a multidimensional Marchenko equation. Besides the reflection data, this methodology requires a background model of the propagation velocity. We present several imaging conditions to retrieve the internal reflectivity of an acoustic medium with correct amplitudes and without artifacts, using the Green’s functions and focusing functions that are derived from the Marchenko equation. We distinguish three types of imaging: 1) imaging by deconvolution, 2) imaging by double focusing, and 3) imaging by cross correlation. In all cases, reflectors can be approached either from above or from below. Imaging by deconvolution or double focusing requires single-sided illumination (meaning that sources and receivers are deployed at a single boundary above the volume only), whereas imaging by cross correlation requires double-sided illumination (meaning that sources and receivers are placed at two boundaries enclosing the volume). In order to achieve double-sided illumination, the required reflection response at the lower boundary can either be physically recorded or it can be retrieved from the reflection response at the upper boundary. When imaging by deconvolution or double focusing, the internal reflectivity is retrieved solely from primary reflections. When imaging by cross correlation, multiple reflections are focused at the image points, such that they contribute physically to the retrieved reflectivity values. This special feature can be beneficial for imaging weakly illuminated sections of strongly heterogeneous media.

**Index Terms**—Image representation, acoustic signal processing.

## I. INTRODUCTION

**I**N ACOUSTIC reflector imaging, we aim to characterize the internal reflectivity of a specific volume by collecting

Manuscript received May 15, 2017; revised October 6, 2017 and November 7, 2017; accepted November 7, 2017. Date of publication November 10, 2017; date of current version February 8, 2018. This work was supported in part by the Dutch Technology Foundation STW, in part by the Applied Science Division of NWO, and in part by the Technology Program of the Ministry of Economic Affairs under Grant VENI.13078. The associate editor coordinating the review of this manuscript and approving it for publication was Prof. Stephen McLaughlin. (*Corresponding author: Joost van der Neut.*)

J. van der Neut is with the Department of Applied Sciences, Laboratory of Acoustical Wavefield Imaging, Delft University of Technology, Delft 2628, The Netherlands (e-mail: j.r.vanderneut@tudelft.nl).

J. Brackenhoff, M. Staring, L. Zhang, E. Slob, and K. Wapenaar are with the Department of Geoscience and Engineering, Section of Applied Geophysics and Petrophysics, Delft University of Technology, Delft 2628, The Netherlands (e-mail: J.A.Brackenhoff@tudelft.nl; M.Staring-2@tudelft.nl; L.Zhang-1@tudelft.nl; e.c.slob@tudelft.nl; c.p.a.wapenaar@tudelft.nl).

S. de Ridder is with the School of Mathematics, University of Edinburgh, Edinburgh EH9 3FD, U.K. (e-mail: s.deridder@ed.ac.uk).

Digital Object Identifier 10.1109/TCI.2017.2772440

the echos from various source and receiver locations outside the volume. The methodology can be applied at various scales, ranging from monitoring the subsurface with low-frequency seismic waves [1] to probing the human body with high-frequency ultrasound [2]. An imaging algorithm is required to retrieve the internal reflectivity of the target volume from the recordings. Most imaging algorithms are based on backpropagation of the acquired data, using Green’s functions in a background model [3]–[5]. Since multiple reflections and transmission effects are not accounted for by this procedure, artifacts can emerge in the image and amplitudes are typically inaccurate. Another limiting factor is that backpropagation methods require a closed boundary of observations [6], [7]. In practice, they are often applied with observations at one side of the volume only, leading to artifacts and inaccurate amplitudes, even if the exact model is used for backpropagation. To overcome these limitations, the internal reflectivity can also be retrieved by inversion [8]. Unfortunately, the underlying inverse problem is typically ill-posed and obtaining a solution is expensive from a computational point of view.

Recently, it has been shown that wavefields inside a volume can be retrieved from observations at a single boundary above the volume by single-sided wavefield focusing [9]. The so-called focusing functions that are required to realize this process can be computed by solving a multidimensional Marchenko equation, which is an extension of its one-dimensional equivalent [10]–[13]. In so-called Marchenko imaging [14], [15], the retrieved wavefields are utilized to obtain an image of the internal reflectivity. Unlike various other methods that are based on closed-boundary representations, Marchenko imaging requires observations at a single boundary only. Since multiple reflections are accounted for by the methodology, image clutter (which is a common problem in seismic data [16] and ultrasound data [17]) is avoided. Reflection clutter appears to be especially significant in photoacoustic imaging [18]–[20]. Hence, we prospect the Marchenko equation to offer fruitful applications for this specific imaging modality [21].

Three steps can be distinguished in Marchenko imaging. In step (1), focusing functions are retrieved from the acquired reflection data. These focusing functions may be interpreted as inverse transmission operators that can propagate the acquired data back into the medium. Actual backpropagation is established in step (2) by convolving the retrieved focusing functions with the reflection data. We refer to this step as single-sided wavefield focusing. We obtain the (up- and downgoing) wave-

fields as they have propagated inside the medium after this operation (given that the acquisition surface is horizontal and located above the volume of interest). In step (3), we obtain an image of the internal reflectivity from the retrieved wavefields. This can be done by solving an inverse problem [22], [23] (this approach is commonly referred to as multidimensional deconvolution). Unfortunately, this process is intensive from a computational point of view. Hence, a range of alternative imaging conditions has been proposed, including crosscorrelation of the up- and downgoing wavefields [24], convolution of the upgoing wavefield with the downgoing focusing function (or its direct part) [25]–[28] and crosscorrelation of the upgoing focusing function with the downgoing wavefield (or its direct part) [14], [29].

In this paper, we evaluate three types of Marchenko imaging conditions, from which most existing imaging strategies can be derived: (1) imaging by deconvolution, (2) imaging by double focusing and (3) imaging by crosscorrelation. In all cases, reflectors can be approached either from above or from below. Unlike in part of the existing literature (where accurate amplitudes are typically ignored in all but deconvolution-based imaging strategies), we strive to retrieve exact reflectivity amplitudes. This is achieved by normalizing the solution of the Marchenko equation. For this purpose, we introduce the concepts of focal normalization and physical normalization in Section II. In Section III, we discuss imaging by deconvolution. For this type of imaging, normalization appears to be irrelevant since deconvolution includes an implicit normalization. Unlike in previous publications, we propose to image the reflected field and the incident field independently and compute their ratio. This procedure saves dramatically on the computation time. In Section IV, we discuss imaging by double focusing. To guarantee accurate amplitudes with this type of imaging, it is essential that physical normalization is applied. In Section V, we continue with imaging by crosscorrelation. We demonstrate that the artifacts that have been reported by [24], [30] and [31] can be avoided if additional data is provided at the bottom of the volume. In order to achieve the desired cancellation of artifacts and the retrieval of accurate amplitudes with this method, we emphasize that physical normalization should be applied.

## II. GENERAL THEORY

We start the paper by reviewing some existing theory. In Section II-A, we present two reciprocity theorems, while we introduce the concepts of Green's functions and focusing functions in Section II-B. In Section II-C, we discuss how the focusing functions can be retrieved by solving the multidimensional Marchenko equation and we show how these focusing functions can be used to compute Green's functions by single-sided wavefield focusing. In Section II-D, we propose two options to normalize the retrieved Green's functions and focusing functions. These normalizations are essential in order to retrieve accurate amplitudes when imaging by double focusing and to allow imaging by crosscorrelation with double-sided illumination. In Section II-E, we summarize the proposed procedure and we discuss how the retrieved wavefields can be used for imaging.

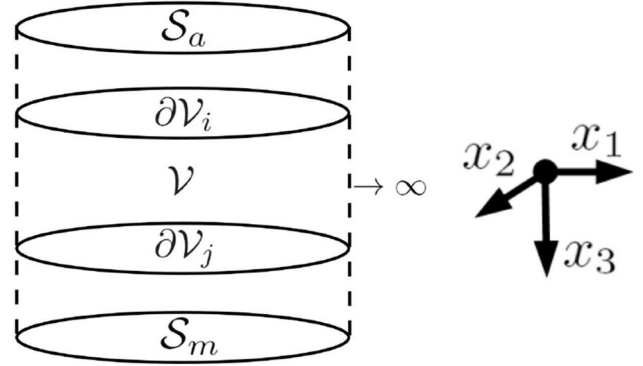


Fig. 1. Configuration that is used in this paper.

### A. Reciprocity Theorems

Wave propagation takes place in a lossless acoustic medium, defined by mass density  $\rho(\mathbf{x})$  and wave velocity  $c(\mathbf{x})$ , where both of which are functions of spatial coordinates  $\mathbf{x} = (x_1, x_2, x_3)$ , with the positive  $x_3$ -axis pointing downwards. In our notation, we use bold symbols to denote multidimensional quantities. A distinction is made between the horizontal coordinates  $\mathbf{x}_H = (x_1, x_2)$  and the vertical coordinate  $x_3$ , which is the preferred direction of wave propagation. Wavefields are described by the pressure  $p(\mathbf{x}, \omega)$  and particle velocity  $\mathbf{v}(\mathbf{x}, \omega) = (v_1(\mathbf{x}, \omega), v_2(\mathbf{x}, \omega), v_3(\mathbf{x}, \omega))$ , which depend on the spatial coordinates and angular frequency. We define the temporal Fourier transform  $f_\omega(\omega)$  of an arbitrary function  $f_t(t)$  of time  $t$  as  $f_\omega(\omega) = \int_{-\infty}^{+\infty} f_t(t) \exp(-j\omega t) dt$ . We decompose the physical quantities  $p(\mathbf{x}, \omega)$  and  $\mathbf{v}(\mathbf{x}, \omega)$  into a downgoing wavefield  $p^+(\mathbf{x}, \omega)$  and an upgoing wavefield  $p^-(\mathbf{x}, \omega)$ , which are normalized with respect to the power flux [32]–[34]. The sources of these wavefields are also decomposed. We recognize a source function for downgoing waves  $s^+(\mathbf{x}, \omega)$  and a source function for upgoing waves  $s^-(\mathbf{x}, \omega)$ .

A multi-source, multi-offset acoustic reflection response is assumed to be recorded at a horizontal surface  $S_a$  at  $x_3 = x_{3a}$ . The medium parameters above this surface are assumed to be constant in the  $x_3$ -direction, such that no downgoing reflections occur in this part of the medium. Another surface  $S_m$  is defined at  $x_3 = x_{3m}$ . The medium parameters below this surface are also assumed to be constant in the  $x_3$ -direction, such that no upgoing reflections occur in this part of the medium. In case of single-sided illumination (i.e. the reflection response is acquired at  $S_a$  only), we may choose  $S_m$  below the lowest discontinuity in the medium by setting  $x_{3m} \rightarrow \infty$ . In case of double-sided illumination,  $x_{3m}$  is finite and additional reflection data is acquired at  $S_m$ . We define a volume  $\mathcal{V}$  inside the medium, which is enclosed by an upper boundary  $\partial\mathcal{V}_i$  at  $x_{3i}$  and a lower boundary  $\partial\mathcal{V}_j$  at  $x_{3j}$ . For this configuration, which is illustrated in Fig. 1, the following reciprocity theorem of the convolution type can be derived [34]:

$$\int_{\mathcal{V}} \{p_A^+ s_B^- - p_A^- s_B^+ + s_A^+ p_B^- - s_A^- p_B^+\} d^3 \mathbf{x} = \int_{\partial\mathcal{V}_j} \{p_A^+ p_B^- - p_A^- p_B^+\} d^2 \mathbf{x} - \int_{\partial\mathcal{V}_i} \{p_A^+ p_B^- - p_A^- p_B^+\} d^2 \mathbf{x}. \quad (1)$$

Similar as in full wavefield reciprocity theorems [35], subscripts  $A$  and  $B$  refer to different states. In each state, we may choose a particular source configuration  $s^\pm$ , leading to an associated wavefield  $p^\pm$ . The medium properties of both states must be the same inside  $\mathcal{V}$  but can be different outside this volume. The formulation can be extended to account for medium parameter contrasts between both states in  $\mathcal{V}$  by including an additional volume integral that describes the interaction of the wavefields with the medium contrasts. We can also derive a reciprocity theorem of the correlation type [34]:

$$\begin{aligned} & \int_{\mathcal{V}} \{p_A^{+*} s_B^+ - p_A^{-*} s_B^- + s_A^{+*} p_B^+ - s_A^{-*} p_B^-\} d^3 \mathbf{x} = \\ & \int_{\partial \mathcal{V}_j} \{p_A^{+*} p_B^+ - p_A^{-*} p_B^-\} d^2 \mathbf{x} - \int_{\partial \mathcal{V}_i} \{p_A^{+*} p_B^+ - p_A^{-*} p_B^-\} d^2 \mathbf{x}, \end{aligned} \quad (2)$$

where superscript  $*$  denotes the complex conjugate. In 2, the evanescent wavefield has been neglected. When the reciprocity theorems are transformed to the time domain by an inverse Fourier transform, the multiplications in 1 and 2 correspond to convolutions and crosscorrelations, respectively. In both theorems, we find a volume integral on the left-hand side that describes the interaction of the wavefields with the source functions. On the right-hand side, we find two integrals over the enclosing boundaries that describe the interaction between wavefields that enter and leave the volume  $\mathcal{V}$  in both states.

### B. Green's Functions and Focusing Functions

We define the one-way Green's function  $G^{\pm\pm'}(\mathbf{x}, \mathbf{x}')$  as the down- or upgoing (superscript  $\pm$ ) response at receiver  $\mathbf{x}$  due to an impulsive down- or upgoing (superscript  $\pm'$ ) source at  $\mathbf{x}'$ . Note that the Green's function is also a function of angular frequency  $\omega$ , which is not explicitly indicated for notational convenience. The superscript  $\pm$  can be evaluated in two modes. In the so-called upper mode, we choose  $\pm \rightarrow +$ . In the lower mode, that is  $\pm \rightarrow -$ . We will also use the superscript  $\mp$ , where  $\mp \rightarrow -$  in the upper mode and  $\mp \rightarrow +$  in the lower mode. In a similar way, the symbols  $\pm'$  and  $\mp'$  can be evaluated in two modes, which we refer to as the upper  $'$  mode and the lower  $'$  mode. By using this compact notation, our expressions can be used for a variety of purposes beyond imaging (for instance acoustic holography [36] or extended imaging [37], [38]). The following relation can be established for source-receiver reciprocity [36]:

$$G^{\pm\pm'}(\mathbf{x}, \mathbf{x}') = \mp \pm' G^{\mp\mp'}(\mathbf{x}', \mathbf{x}). \quad (3)$$

This equation can be evaluated in four modes. In the upper-upper  $'$  mode, we find  $G^{++}(\mathbf{x}, \mathbf{x}') = -G^{--}(\mathbf{x}', \mathbf{x})$ . In the lower-lower  $'$  mode, that is  $G^{--}(\mathbf{x}, \mathbf{x}') = -G^{++}(\mathbf{x}', \mathbf{x})$ , while in the lower-upper  $'$ - and upper-lower  $'$  mode, we find  $G^{-+}(\mathbf{x}, \mathbf{x}') = G^{-+}(\mathbf{x}', \mathbf{x})$  and  $G^{+-}(\mathbf{x}, \mathbf{x}') = G^{+-}(\mathbf{x}', \mathbf{x})$ , respectively.

Apart from the Green's function, we also define a focusing function  $f_1^\pm(\mathbf{x}, \mathbf{x}')$  (where superscript  $\pm$  denotes downgoing and upgoing at  $\mathbf{x}$  in the upper and lower mode, respectively). The focusing function depends on angular frequency  $\omega$  (which is not indicated explicitly in the argument list), location  $\mathbf{x}$  and

TABLE I  
DEFINITIONS OF TRUNCATED MEDIA 1 AND 2

| Interval       | Medium 1                                              | Medium 2                                              |
|----------------|-------------------------------------------------------|-------------------------------------------------------|
|                | $c_1(\mathbf{x}_H, x_3), \rho_1(\mathbf{x}_H, x_3)$   | $c_2(\mathbf{x}_H, x_3), \rho_2(\mathbf{x}_H, x_3)$   |
| $x_3 < x_{3t}$ | $c(\mathbf{x}_H, x_3), \rho(\mathbf{x}_H, x_3)$       | $c(\mathbf{x}_H, x_{3t}), \rho(\mathbf{x}_H, x_{3t})$ |
| $x_3 = x_{3t}$ | $c(\mathbf{x}_H, x_{3t}), \rho(\mathbf{x}_H, x_{3t})$ | $c(\mathbf{x}_H, x_{3t}), \rho(\mathbf{x}_H, x_{3t})$ |
| $x_3 > x_{3t}$ | $c(\mathbf{x}_H, x_{3t}), \rho(\mathbf{x}_H, x_{3t})$ | $c(\mathbf{x}_H, x_3), \rho(\mathbf{x}_H, x_3)$       |

the so-called focal point  $\mathbf{x}'$ . The function is defined in truncated medium 1, whose medium properties are illustrated in Table I. Note that this medium is identical to the physical medium above a truncation level  $x_{3t}$ . However, since the medium parameters are not varying in the  $x_3$ -direction below this level, no upgoing reflections occur in this part of the medium. The truncation level coincides with the focal point, i.e.  $x_{3t} = x'_3$ . The focusing function focuses at the focal point, which is specified by the focusing condition [15]:

$$f_1^\pm(\mathbf{x}, \mathbf{x}')|_{x_3=x'_3} = \chi^0 \delta(\mathbf{x}_H - \mathbf{x}'_H), \quad (4)$$

where  $\delta(\mathbf{x}_H) = \delta(x_1) \delta(x_2)$  is a 2D Dirac-delta function. In this expression, we have defined the function  $\chi^0$ , where  $\chi^0 = 1$  in the upper mode and  $\chi^0 = 0$  in the lower mode.

We introduce another focusing function  $f_2^\pm(\mathbf{x}, \mathbf{x}'')$  which focuses a wavefield from below at an arbitrary focal point  $\mathbf{x}''$ . This function is defined in truncated medium 2, which is also specified in Table I. Truncated medium 2 is identical to the physical medium below the truncation level  $x_{3t}$ . However, since the medium parameters are not varying in the  $x_3$ -direction above this level, no downgoing reflections occur in this part of the medium. Once again, the truncation level coincides with the focal point, i.e.  $x_{3t} = x''_3$ . This focusing function obeys the following focusing condition [15]:

$$f_2^\pm(\mathbf{x}, \mathbf{x}'')|_{x_3=x''_3} = \chi^0 \delta(\mathbf{x}_H - \mathbf{x}''_H), \quad (5)$$

where  $\chi^0 = 0$  in the upper mode and  $\chi^0 = 1$  in the lower mode.

### C. The Marchenko Operator and Single-Sided Focusing

The focusing functions that are required for imaging can be retrieved by solving a multidimensional Marchenko equation [15]. This procedure requires knowledge of the medium's reflection response from the upper acquisition surface  $\mathcal{S}_a$  and an estimate of an initial propagator, which we refer to as  $d(\mathbf{x}, \mathbf{x}_a)$ . The initial propagator is formally defined as the inverse of the direct wavefield as it propagates from a source  $\mathbf{x}_a \in \mathcal{S}_a$  to each location  $\mathbf{x}$  in the medium [9]. The solution of the multidimensional Marchenko equation can be expressed as a linear operator  $\mathcal{M}_1^\pm$  which acts on  $d(\mathbf{x}, \mathbf{x}_a)$ , according to

$$f_1^\pm(\mathbf{x}_a, \mathbf{x}) = \{\mathcal{M}_1^\pm d\}(\mathbf{x}, \mathbf{x}_a). \quad (6)$$

Operator  $\mathcal{M}_1^\pm$  is constructed by successive application of an operator for crosscorrelation with the reflection response (where an integral over the acquisition surface is to be evaluated) and an operator that truncates signals in the time domain. This construction can be realized if the medium is characterized by smoothly varying interfaces [15]. Approximate solutions can be found in

media with sharp contrasts such as diffractors [39]. For explicit definitions of  $\mathcal{M}_1^-$  and  $\mathcal{M}_1^+$ , we refer to equations 32 and 33 in [39], respectively. The second kind of focusing function  $f_2$  can be obtained from  $f_1$  by using the following symmetry relations [15]:  $f_2^+(\mathbf{x}, \mathbf{x}_a) = -f_1^{-*}(\mathbf{x}_a, \mathbf{x})$  and  $f_2^-(\mathbf{x}, \mathbf{x}_a) = f_1^+(\mathbf{x}_a, \mathbf{x})$ . Note that  $f_1^+(\mathbf{x}_a, \mathbf{x})$  and  $f_1^-(\mathbf{x}_a, \mathbf{x})$  are defined in truncated medium 1, which is reflection-free below  $\mathbf{x}$ , while  $f_2^+(\mathbf{x}, \mathbf{x}_a)$  and  $f_2^-(\mathbf{x}, \mathbf{x}_a)$  are defined in truncated medium 2, which is reflection-free above  $\mathbf{x}_a$ . Both focusing functions are independent on the part of the medium above  $\mathbf{x}_a$  and on the part below  $\mathbf{x}$ .

Once the focusing functions are retrieved, they can be convolved with the reflection response  $R^+(\mathbf{x}_a, \mathbf{x}'_a) = G^{-+}(\mathbf{x}_a, \mathbf{x}'_a)$  at the acquisition surface  $\mathcal{S}_a$  (with  $\mathbf{x}'_a \in \mathcal{S}_a$ ) to realize single-sided wavefield focusing. The upgoing Green's function can be retrieved by the following representation [14], [15], [39]:

$$G^{-+}(\mathbf{x}, \mathbf{x}_a) = \int_{\mathcal{S}_a} R^+(\mathbf{x}_a, \mathbf{x}'_a) f_1^+(\mathbf{x}'_a, \mathbf{x}) d^2 \mathbf{x}'_a - f_1^-(\mathbf{x}_a, \mathbf{x}). \quad (7)$$

An equivalent representation can be derived for the downgoing Green's function:

$$G^{++}(\mathbf{x}, \mathbf{x}_a) = - \int_{\mathcal{S}_a} R^+(\mathbf{x}_a, \mathbf{x}'_a) f_1^{-*}(\mathbf{x}'_a, \mathbf{x}) d^2 \mathbf{x}'_a + f_1^{+*}(\mathbf{x}_a, \mathbf{x}). \quad (8)$$

In practice, the acquired reflection data that is used to compute the Marchenko operators is bandlimited. This poses a limitation to the resolution of the methodology. To account for the finite bandwidth of the data, the initial propagator  $d(\mathbf{x}, \mathbf{x}_a)$  must have been convolved with a zero-phase wavelet  $S(\omega)$ , which is non-zero only inside the interval  $[-t^S, t^S]$ . Consequently, contrasts with a thickness less than  $ct^S$  (where  $c$  is the velocity of the contrast) cannot be distinguished by the methodology [14].

#### D. Normalization

The initial propagator  $d(\mathbf{x}, \mathbf{x}_a)$  is typically approximated by a time-reversed wavefield, which is computed in a smooth background model [22]. Unfortunately, transmission effects are not accounted for in this estimate, posing limitations for some of the imaging conditions derived herein. For some methods, it can be beneficial to scale the initial propagator by enforcing that for any  $\mathbf{x}$

$$\int_{-\infty}^{+\infty} \int_{\mathcal{S}_a} \frac{|S|^2}{2\pi} d^*(\mathbf{x}, \mathbf{x}_a) d(\mathbf{x}, \mathbf{x}_a) d^2 \mathbf{x}_a d\omega = A. \quad (9)$$

Here,  $|S|^2$  is the power spectrum of the source wavelet and  $A$  is a constant. To account for the finite temporal and spatial band limitation, we define  $A$  proportional to the multidimensional autocorrelation of a propagator in a homogeneous medium, which is equivalent to the spatial-temporal resolution function for seismic migration [40]. For wave propagation in 3D media, this

leads to the following definition for  $A$ :

$$A = \lim_{r \rightarrow 0} \int_{-\infty}^{+\infty} \frac{|S|^2 |\omega| J_1(|\omega| r / c_a)}{4\pi^2 c_a r} d\omega = \int_{-\infty}^{+\infty} \frac{|S|^2 |\omega|^2}{8\pi^2 c_a^2} d\omega, \quad (10)$$

where  $r = \sqrt{x_1^2 + x_2^2}$  and  $J_1$  is a Bessel function of the first kind. Further we defined the apparent velocity as  $c_a = c / \sin(\alpha_{\max})$ , where  $\alpha_{\max}$  denotes the maximum propagation angle that is covered by the acquisition array. For 2D wave propagation, we find equivalently

$$A_{2D} = \lim_{x_1 \rightarrow 0} \int_{-\infty}^{+\infty} \frac{|S|^2 \sin\left(\frac{|\omega| x_1}{c_a}\right)}{2\pi^2 x_1} d\omega = \int_{-\infty}^{+\infty} \frac{|S|^2 |\omega|}{2\pi^2 c_a} d\omega, \quad (11)$$

whereas for 1D wave propagation:

$$A_{1D} = \int_{-\infty}^{+\infty} \frac{|S|^2}{2\pi} d\omega. \quad (12)$$

If our initial propagators obey 9, we speak of focal normalization. The amplitudes of the retrieved Green's functions and focusing functions, however, are incorrect when this kind of normalization is applied. To retrieve accurate amplitudes, we require a different normalization. This can be established by enforcing that  $d(\mathbf{x}, \mathbf{x}_a)$  is proportional to the inverse of the direct part of the Green's function, which is retrieved when 6 and 8 are evaluated. The direct part of the Green's function can be written as  $G_d^{++}(\mathbf{x}, \mathbf{x}_a) = \{\Theta_d G^{++}\}(\mathbf{x}, \mathbf{x}_a)$ , where  $\Theta_d$  is an operator that isolates the direct wavefield from the downgoing Green's function  $G^{++}(\mathbf{x}, \mathbf{x}_a)$  (which is retrieved by 8). By enforcing that for any  $\mathbf{x}$  [41]

$$\int_{-\infty}^{+\infty} \int_{\mathcal{S}_a} \frac{|S|^2}{2\pi} G_d^{++}(\mathbf{x}, \mathbf{x}_a) d(\mathbf{x}, \mathbf{x}_a) d^2 \mathbf{x}_a d\omega = A, \quad (13)$$

we can guarantee amplitudes of  $d(\mathbf{x}, \mathbf{x}_a)$  and the retrieved Green's functions / focusing functions to be relatively accurate. Note that this condition is only valid if the decomposed wavefields are normalized with respect to the powerflux, as we assume in this paper. For so-called pressure-normalized wavefields, physical normalization is less trivial and requires knowledge of the medium properties at the focal point (see [15], appendix A). We can use 13 to rescale the amplitudes of an initial propagator  $d(\mathbf{x}, \mathbf{x}_a)$ , which was originally computed in a smooth background model. In 1D, this can be done by solving a simple (but non-linear) minimization problem [41]. Currently, we are extending this methodology to 2D and 3D. When 13 is obeyed, we speak of so-called physical normalization.

#### E. Marchenko Imaging

In this paper, we derive several representations for Marchenko imaging. A general flowchart for this process is provided in Fig. 2. Starting with an initial propagator that is computed in a background model, we compute the focusing functions and Green's functions with 6, 7 and 8. Then, we rescale the initial propagator by enforcing that either 9 or 13 is satisfied. After recomputing the Green's functions and focusing functions, the wavefields can be imaged by either (1) deconvolution, (2) double focusing or (3) crosscorrelation. In the following sections, we discuss imaging conditions for each of these strategies.

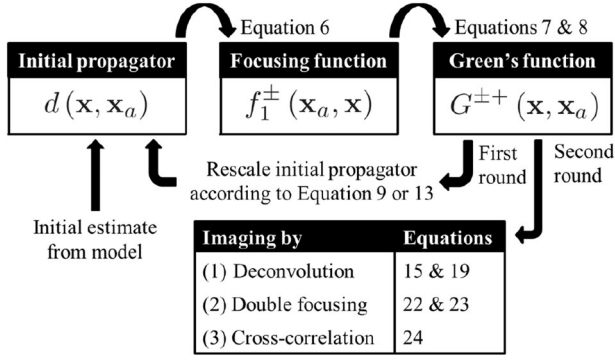


Fig. 2. Proposed flowchart for Marchenko imaging.

TABLE II  
WAVEFIELDS FOR IMAGING BY DECONVOLUTION WHEN REFLECTORS ARE APPROACHED FROM ABOVE

| Field | State A                             | State B                                                                           |
|-------|-------------------------------------|-----------------------------------------------------------------------------------|
| $p^+$ | $G^{++}(\mathbf{x}, \mathbf{x}_a)$  | $G_2^{+\mp}(\mathbf{x}, \mathbf{x}_q) = \pm G_2^{\pm-}(\mathbf{x}_q, \mathbf{x})$ |
| $p^-$ | $G^{-+}(\mathbf{x}, \mathbf{x}_a)$  | $G_2^{-\mp}(\mathbf{x}, \mathbf{x}_q) = \mp G_2^{\pm+}(\mathbf{x}_q, \mathbf{x})$ |
| $s^+$ | $\delta(\mathbf{x} - \mathbf{x}_a)$ | $\chi_0^1 \delta(\mathbf{x} - \mathbf{x}_q)$                                      |
| $s^-$ | 0                                   | $\chi_0^1 \delta(\mathbf{x} - \mathbf{x}_q)$                                      |

### III. IMAGING BY DECONVOLUTION

Once the up- and downgoing Green's functions and focusing functions are retrieved inside the volume of interest, we can redatum the sources into that volume by so-called multidimensional deconvolution [15], [22]. By integrating the result over frequency, an image can be obtained with accurate amplitudes without artifacts from multiple reflections. In Section III-A and III-B, we show how this can be done by approaching medium contrasts from above and from below, respectively. In Section III-C, we illustrate these imaging strategies with 1D examples.

#### A. Approaching Reflectors From Above

We assume that reflection data are collected at the upper acquisition surface  $\mathcal{S}_a$ . To approach contrasts in the medium from above at an arbitrary location  $\mathbf{x}_e$  in the medium, we choose the upper boundary  $\partial\mathcal{V}_i$  of volume  $\mathcal{V}$  such that  $\mathbf{x}_e \in \partial\mathcal{V}_i$ . The lower boundary of  $\mathcal{V}$  is placed at the bottom of the medium, such that  $\partial\mathcal{V}_j = \mathcal{S}_m$ . In state A, we choose a downgoing source at  $\mathbf{x}_a \in \mathcal{S}_a$ , which is located above volume  $\mathcal{V}$ . In state B, we place a source at  $\mathbf{x}_q \in \mathcal{V}$  in truncated medium 2 (see Table I), where the truncation is applied at  $x_{3t} = x_{3i}$ . The source function is upgoing in the upper mode and downgoing in the lower mode. The resulting wavefields are shown in Table II, where subscript 2 denotes the truncated medium and source-receiver reciprocity relation 3 has been applied. By substituting these wavefields into the reciprocity theorem of the convolution type 1, it can be derived that

$$G^{\pm+}(\mathbf{x}_q, \mathbf{x}_a) = \int_{\partial\mathcal{V}_i} G_2^{\pm+}(\mathbf{x}_q, \mathbf{x}) G^{++}(\mathbf{x}, \mathbf{x}_a) d^2\mathbf{x}. \quad (14)$$

Given that  $G^{\pm+}(\mathbf{x}_q, \mathbf{x}_a)$  and  $G^{++}(\mathbf{x}, \mathbf{x}_a)$  can be computed from reflection data at  $\mathcal{S}_a$  by solving the multidimensional Marchenko equation, the unknown quantity  $G_2^{\pm+}(\mathbf{x}_q, \mathbf{x})$  can be retrieved from 14 by least-squares inversion. This can be done in either the upper mode (i.e.  $\pm \rightarrow +$ ) or in the lower mode (i.e.  $\pm \rightarrow -$ ). If we let  $\mathbf{x}_q$  approach an image point  $\mathbf{x}_e \in \partial\mathcal{V}_i$  in the limit from below in the lower mode, we find a spatially band limited version of  $G_2^{-+}(\mathbf{x}_e, \mathbf{x}_e)$ . When we integrate this quantity over frequency, the result can be directly related to the reflectivity  $r^+(\mathbf{x}_e)$  at the image point [42]. By repeating this exercise at each image point in the volume, an image of the internal reflectivity can be constructed [22].

Unfortunately, least-squares inversion of 14 is computationally very expensive. To save on the computational burden, we suggest to convolve both sides of 14 spatially with the initial propagator  $d(\mathbf{x}_p, \mathbf{x}_a)$  at a location  $\mathbf{x}_p \in \partial\mathcal{V}_i$  and to integrate over  $\mathbf{x}_a$ . Moreover, we multiply both sides of the equation with the power spectrum of the source wavelet  $|S|^2$  to take finite temporal bandwidth into account. After changing the order of integration, we arrive at

$$\Gamma^{\pm+}(\mathbf{x}_q, \mathbf{x}_p) = \int_{\partial\mathcal{V}_i} G_2^{\pm+}(\mathbf{x}_q, \mathbf{x}) \Gamma^{++}(\mathbf{x}, \mathbf{x}_p) d^2\mathbf{x}, \quad (15)$$

where we have defined

$$\Gamma^{\pm+}(\mathbf{x}, \mathbf{x}_p) = \int_{\mathcal{S}_a} |S|^2 G^{\pm+}(\mathbf{x}, \mathbf{x}_a) d(\mathbf{x}_p, \mathbf{x}_a) d^2\mathbf{x}_a. \quad (16)$$

We may let  $\mathbf{x}_q$  approach  $\mathbf{x}_e$  in the limit from below and set  $\mathbf{x}_p = \mathbf{x}_e$ . If we integrate  $\Gamma^{-+}(\mathbf{x}_e, \mathbf{x}_e)$  and  $\Gamma^{++}(\mathbf{x}_e, \mathbf{x}_e)$  independently over frequency (which is equivalent to inverse Fourier transformation and evaluating the result at zero time), we can obtain the reflected amplitude  $a_{\Gamma}^{-+}(\mathbf{x}_e)$  and incident amplitude  $a_{\Gamma}^{++}(\mathbf{x}_e)$ , respectively. When we take the ratio of these scalar quantities  $a_{\Gamma}^{-+}(\mathbf{x}_e)/a_{\Gamma}^{++}(\mathbf{x}_e)$ , the result is proportional to the internal reflectivity  $r^+(\mathbf{x}_e)$ . The computational cost of this operation is dramatically less than the cost of least-squares inversion, since solving a large-scale inverse problem has been replaced by a simple scalar division. The accuracy of this imaging condition in 2D and 3D media is still to be investigated.

The up- and downgoing Green's functions that are retrieved with 7 and 8 depend linearly on amplitude errors in the initial propagators  $d(\mathbf{x}, \mathbf{x}_a)$ . Hence, these errors cancel each other when the ratio  $a_{\Gamma}^{-+}(\mathbf{x}_e)/a_{\Gamma}^{++}(\mathbf{x}_e)$  is computed. As a consequence, deconvolution-based imaging is not very sensitive to these errors, which is an important advantage of this methodology. Finally, we note that the downgoing Green's function  $G^{++}(\mathbf{x}, \mathbf{x}_a)$  can be expressed as a superposition of a direct part  $G_d^{++}(\mathbf{x}, \mathbf{x}_a)$  and a coda  $G_m^{++}(\mathbf{x}, \mathbf{x}_a)$ . Consequently, we find for the incident amplitude:

$$\begin{aligned} a_{\Gamma}^{++}(\mathbf{x}_e) &= \int_{-\infty}^{+\infty} \int_{\mathcal{S}_a} \frac{|S|^2}{2\pi} G_d^{++}(\mathbf{x}_e, \mathbf{x}_a) d(\mathbf{x}_e, \mathbf{x}_a) d^2\mathbf{x}_a d\omega \\ &\quad + \int_{-\infty}^{+\infty} \int_{\mathcal{S}_a} \frac{|S|^2}{2\pi} G_m^{++}(\mathbf{x}_e, \mathbf{x}_a) d(\mathbf{x}_e, \mathbf{x}_a) d^2\mathbf{x}_a d\omega. \end{aligned} \quad (17)$$

TABLE III  
WAVEFIELDS FOR IMAGING BY DECONVOLUTION WHEN REFLECTORS ARE APPROACHED FROM BELOW

| Field | State A                           | State B                                                                                  |
|-------|-----------------------------------|------------------------------------------------------------------------------------------|
| $p^+$ | $f_2^+(\mathbf{x}, \mathbf{x}_a)$ | $G_{1(x_3)}^{+\mp}(\mathbf{x}, \mathbf{x}_q) = \pm G_1^{\pm-}(\mathbf{x}_q, \mathbf{x})$ |
| $p^-$ | $f_2^-(\mathbf{x}, \mathbf{x}_a)$ | $G_{1(x_3)}^{-\mp}(\mathbf{x}, \mathbf{x}_q) = \mp G_1^{\pm+}(\mathbf{x}_q, \mathbf{x})$ |
| $s^+$ | 0                                 | $\chi_1^0 \delta(\mathbf{x} - \mathbf{x}_q)$                                             |
| $s^-$ | 0                                 | $\chi_1^0 \delta(\mathbf{x} - \mathbf{x}_q)$                                             |

Remember that integration over frequency can be interpreted as inverse Fourier transformation and evaluating the result at zero time. Since the coda arrives after the direct wavefield by definition, the second integral has no contribution at zero time and vanishes (where we assume that the support of the wavelet is sufficiently compact). Note that the first integral is equivalent to left-hand side of 13 (after substitution of  $\mathbf{x} = \mathbf{x}_e$ ). Consequently,  $a_{\Gamma}^{++}(\mathbf{x}_e)$  is constant if physical normalization is enforced, such that  $a_{\Gamma}^{++}(\mathbf{x}_e)$  will be proportional to the reflectivity  $r^+(\mathbf{x}_e)$ . Therefore, an image can be constructed directly by evaluating  $a_{\Gamma}^{++}(\mathbf{x}_e)$  at each image point  $\mathbf{x}_e$  in this case.

### B. Approaching Reflectors From Below

By using the focusing functions rather than Green's functions, we can approach reflectors from below (given that data are collected from above). Because of the finite temporal resolution of the reflection data, the reflectivity at an arbitrary image point  $\mathbf{x}_e$  is not included in the focusing function at  $\mathbf{x}_e$  [39]. Therefore, we have to evaluate the Marchenko equation at  $\mathbf{x}_e^{+\epsilon}$  at a distance  $c(\mathbf{x}_e^{+\epsilon})t^\epsilon$  below the actual image point, satisfying  $\mathbf{x}_e^{+\epsilon} = (\mathbf{x}_{He}, x_{3e} + c(\mathbf{x}_e^{+\epsilon})t^\epsilon)$ . In this formulation,  $t^\epsilon$  is a time step that depends on the frequency band of the available data and  $c(\mathbf{x}_e^{+\epsilon})$  is the velocity at  $\mathbf{x}_e^{+\epsilon}$ , which can be obtained from the background model. A convenient choice is  $t^\epsilon = t^S$ , where  $t^S$  depends on the wavelet that is used to solve the Marchenko equation and has been defined earlier in this paper. By this choice, we account for the finite temporal resolution of the Marchenko equation [14]. To derive a representation for this scenario, we let the upper boundary of volume  $\mathcal{V}$  coincide with the acquisition surface, i.e.  $\partial\mathcal{V}_i = \mathcal{S}_a$ . We choose the lower boundary  $\partial\mathcal{V}_j$  such that  $\mathbf{x}_e^{+\epsilon} \in \partial\mathcal{V}_j$ . In state A, we define focusing function  $f_2$  with a focal point at  $\mathbf{x}_a \in \mathcal{S}_a$ . In state B, we choose a source at  $\mathbf{x}_q \in \mathcal{V}$ , radiating upwards in the upper mode and downwards in the lower mode. The constructed wavefields are given in Table III (in this table, subscript 1 ( $x_3$ ) means that the medium is truncated at  $x_{3t} = x_3$  rather than at the source location). When we substitute these quantities into the reciprocity theorem of the convolution type 1, we find

$$f_2^\pm(\mathbf{x}_q, \mathbf{x}_a) = - \int_{\partial\mathcal{V}_j} G_1^{\pm-}(\mathbf{x}_q, \mathbf{x}) f_2^-(\mathbf{x}, \mathbf{x}_a) d^2\mathbf{x}. \quad (18)$$

If we evaluate this expression with  $\mathbf{x}_q$  approaching  $\mathbf{x}_e^{+\epsilon}$  in the limit from above in the upper mode,  $G_1^{+-}(\mathbf{x}_e^{+\epsilon}, \mathbf{x}_e^{+\epsilon})$  can be retrieved for every image point  $\mathbf{x}_e$  in the medium by least-squares inversion. We can extrapolate this wavefield

to the image point  $\mathbf{x}_e$  with a two-way (at the source and receiver side) extrapolation operator  $\mathcal{E}(t^\epsilon, c(\mathbf{x}_e^{+\epsilon}))$ , using the local velocity at  $\mathbf{x}_e^{+\epsilon}$ . This yields  $G_1^{+-}(\mathbf{x}_e, \mathbf{x}_e) \approx \{\mathcal{E}(t^\epsilon, c(\mathbf{x}_e^{+\epsilon})) G_1^{+-}\}(\mathbf{x}_e^{+\epsilon}, \mathbf{x}_e^{+\epsilon})$ . In 1D, we can replace the action of the extrapolator with a simple time shift, according to  $G_1^{+-}(\mathbf{x}_e, \mathbf{x}_e) \approx \exp(2j\omega t^\epsilon) G_1^{+-}(\mathbf{x}_e^{+\epsilon}, \mathbf{x}_e^{+\epsilon})$ . In 2D and 3D, we may prefer to use a multidimensional extrapolator [40]. If we integrate the extrapolated wavefield  $\{\mathcal{E}(t^\epsilon, c(\mathbf{x}_e^{+\epsilon})) G_1^{+-}\}(\mathbf{x}_e^{+\epsilon}, \mathbf{x}_e^{+\epsilon})$  over frequency, the result will be proportional to the reflectivity from below  $r^-(\mathbf{x}_a)$ .

Once again, the retrieval of  $G_1^{+-}(\mathbf{x}_e^{+\epsilon}, \mathbf{x}_e^{+\epsilon})$  by least-squares inversion is expensive from a computational point of view. As an alternative, we may multiply both sides of 18 with  $d^*(\mathbf{x}_p, \mathbf{x}_a)$  with  $\mathbf{x}_p \in \partial\mathcal{V}_j$  and integrate  $\mathbf{x}_a$  over the acquisition surface  $\mathcal{S}_a$ . We also multiply both sides of the equation with the power spectrum of the source wavelet  $|S|^2$  to take finite temporal bandwidth into account. After changing the order of integration, we arrive at

$$\Gamma^{\pm-}(\mathbf{x}_q, \mathbf{x}_p) = - \int_{\partial\mathcal{V}_j} G_1^{\pm-}(\mathbf{x}_q, \mathbf{x}) \Gamma^{\mp-}(\mathbf{x}, \mathbf{x}_p) d^2\mathbf{x}, \quad (19)$$

with

$$\Gamma^{\pm-}(\mathbf{x}, \mathbf{x}_p) = \int_{\mathcal{S}_a} |S|^2 f_2^\pm(\mathbf{x}, \mathbf{x}_a) d^*(\mathbf{x}_p, \mathbf{x}_a) d^2\mathbf{x}_a. \quad (20)$$

We may evaluate these results with  $\mathbf{x}_q$  approaching  $\mathbf{x}_e^{+\epsilon}$  in the limit from above and setting  $\mathbf{x}_p = \mathbf{x}_e^{+\epsilon}$  in the upper mode. The incident amplitude  $a_{\Gamma}^-(\mathbf{x}_e)$  can be computed by integrating  $\Gamma^{\mp-}(\mathbf{x}_e^{+\epsilon}, \mathbf{x}_e^{+\epsilon})$  over frequency. For the reflected amplitude  $a_{\Gamma}^{+-}(\mathbf{x}_e)$ , we can integrate  $\{\mathcal{E}(t^\epsilon, c(\mathbf{x}_e^{+\epsilon})) \Gamma^{\mp-}\}(\mathbf{x}_e^{+\epsilon}, \mathbf{x}_e^{+\epsilon})$  (where  $\mathcal{E}$  is the two-way inverse wavefield extrapolator that we discussed before) over frequency. The reflectivity from below  $r^-(\mathbf{x}_e)$  can be estimated by computing the ratio  $a_{\Gamma}^{+-}(\mathbf{x}_e)/a_{\Gamma}^-(\mathbf{x}_e)$ . Finally, we note that the upgoing focusing function  $f_2^-(\mathbf{x}, \mathbf{x}_a)$  can be expressed as a superposition of a direct part  $d(\mathbf{x}, \mathbf{x}_a)$  and a coda  $m(\mathbf{x}, \mathbf{x}_a)$ . Consequently, the incident amplitude can be written as

$$a_{\Gamma}^-(\mathbf{x}_e) = \int_{-\infty}^{+\infty} \int_{\mathcal{S}_a} \frac{|S|^2}{2\pi} d(\mathbf{x}_e^{+\epsilon}, \mathbf{x}_a) d^*(\mathbf{x}_e^{+\epsilon}, \mathbf{x}_a) d^2\mathbf{x}_a d\omega \\ + \int_{-\infty}^{+\infty} \int_{\mathcal{S}_a} \frac{|S|^2}{2\pi} m(\mathbf{x}_e^{+\epsilon}, \mathbf{x}_a) d^*(\mathbf{x}_e^{+\epsilon}, \mathbf{x}_a) d^2\mathbf{x}_a d\omega. \quad (21)$$

Because the coda arrives after the direct wavefield by definition, the second integral has no contribution at zero time and vanishes. The remaining integral is equivalent to the left-hand side of 9 (after substitution of  $\mathbf{x} = \mathbf{x}_e^{+\epsilon}$ ). Hence, the incident amplitude  $a_{\Gamma}^-(\mathbf{x}_e)$  is constant when focal normalization is enforced, such that  $a_{\Gamma}^-(\mathbf{x}_e)$  is directly proportional to the local reflectivity from below  $r^-(\mathbf{x}_e)$ . Since focal normalization is relatively easy to apply, this is considered to be an attractive way to image the medium, especially in 1D [14].

### C. Examples

We illustrate imaging by deconvolution with a 1D synthetic example, where  $x_3$  denotes the spatial dimension. In

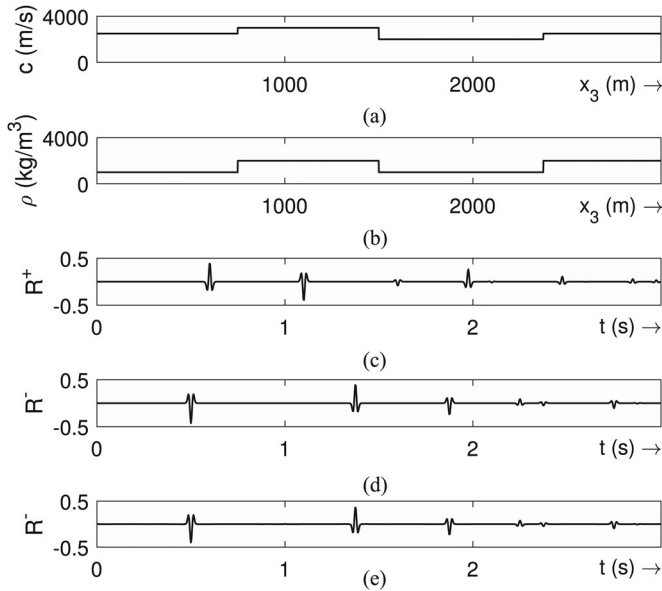


Fig. 3. Synthetic model and data. Model of (a) propagation velocity  $c(x_3)$  and (b) density  $\rho(x_3)$ . (c) Reflection response from above  $R^+(t)$  at  $x_{3a}$ . (d) Reflection response from below  $R^-(t)$  at  $x_{3m}$ . In (e) we show the reflection response from below as retrieved from the reflection response from above, using the procedure that is outlined in the main text.

Fig. 3(a) and (b), we show a velocity and a density model, respectively. These models contain 3001 samples with spacing  $dx_3 = 1$  m. We let  $\mathcal{S}_a$  and  $\mathcal{S}_m$  coincide with the boundaries  $x_{3a} = 0$  m and  $x_{3m} = 3000$  m, respectively. Three contrasts can be distinguished at 750 m, 1500 m and 2375 m, with reflectivity values  $r^+(750) = 0.42$ ,  $r^+(1500) = -0.50$  and  $r^+(2375) = 0.43$ , respectively. These values have been computed with the relation  $r^+(x_3) = \frac{Z(x_3+dx_3) - Z(x_3-dx_3)}{Z(x_3+dx_3) + Z(x_3-dx_3)}$  [43], where  $Z(x_3) = c(x_3)\rho(x_3)$  is the acoustic impedance. Reflectivity values from below have also been computed, with help of the relation  $r^-(x_3) = -r^+(x_3)$  [43]. Our objective is to reconstruct these reflectivity values with accurate amplitudes and without artifacts. In Fig. 3(c) and (d), the reflection responses at  $x_{3a}$  and  $x_{3m}$  are shown, which are used to compute the Marchenko operators. These reflection responses have been convolved with the wavelet  $S(\omega) = \frac{2\omega^2}{\sqrt{\pi}\omega_p^3} \exp(-\frac{\omega^2}{\omega_p^2})$ , with  $\omega_p = 2\pi f_p$ , where  $f_p = 30$  Hz is the peak frequency. In the geophysical community, this is also known as a 30 Hz Ricker wavelet [44]. We have used 2048 time samples with  $dt = 3.4$  ms sampling. Further, we define  $t^e = t^s = 51$  ms. As discussed before, the reflection response at  $x_{3m}$  can also be computed by evaluating the Marchenko equation with the data at  $x_{3a}$  and solving 18 in the upper mode at  $x_{3j} = x_{3m}$ . In Fig. 3(e), we validate that this procedure leads indeed to the required reflection response at  $x_{3m}$ .

We compute Green's functions and focusing functions at all image points under focal normalization (meaning that 9 is satisfied) from the reflection response at  $x_{3a}$ . In Fig. 4(a), we show the reflected amplitude  $a_{\Gamma}^{-+}(x_{3e})$ . We can recognize the three interfaces of the model. However, the amplitudes of the deeper reflections are underestimated, as can be seen by the horizontal bars that indicate the reflectivity values that we have computed

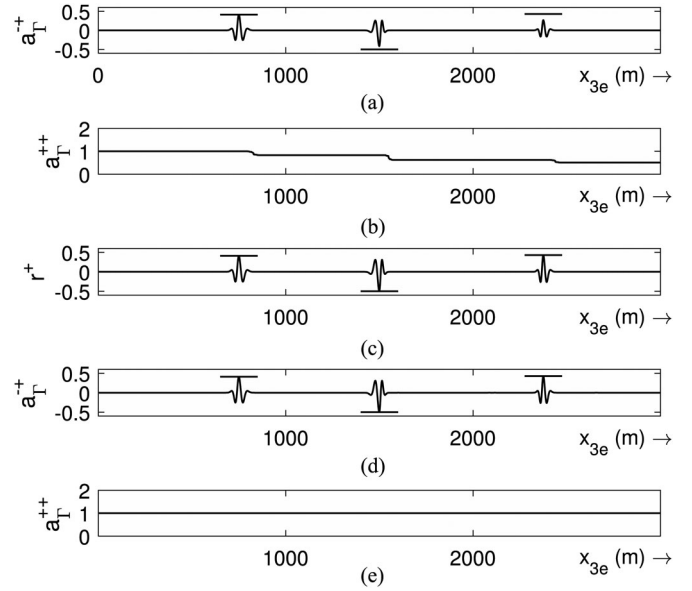


Fig. 4. Imaging by deconvolution from above. (a) Reflected amplitude  $a_{\Gamma}^{-+}(x_{3e})$ , (b) incident amplitude  $a_{\Gamma}^{++}(x_{3e})$  and (c) their ratio (i.e. the reflectivity from above  $r^+(x_{3e})$ ) under focal normalization. (d) Reflected amplitude  $a_{\Gamma}^{-+}(x_{3e})$  and (e) incident amplitude  $a_{\Gamma}^{++}(x_{3e})$  under physical normalization. The horizontal bars indicate the reflectivity values (computed directly from the model parameters) for reference.

from the model parameters. This mismatch can be explained by the fact that transmission effects have not (yet) been accounted for. These transmission effects are described by the incident amplitude  $a_{\Gamma}^{++}(x_{3e})$ , which is shown in Fig. 4(b). By taking the ratio of the reflected and the incident amplitude, we find the reflectivity from above  $r^+(x_{3e})$ , see Fig. 4(c). Note that the reflectivity values are indeed better resolved after this procedure. When the Green's functions and focusing functions are computed under physical normalization (meaning that 13 is satisfied), the reflectivity can be obtained directly from the reflected amplitude  $a_{\Gamma}^{-+}(x_{3e})$ , as illustrated in Fig. 4(d). Since the incident amplitude  $a_{\Gamma}^{++}(x_{3e}) = 1$  in this case [see Fig. 4(e)], it follows that the reflected amplitude  $a_{\Gamma}^{-+}(x_{3e})$  is directly proportional to the reflectivity from above.

The reflectors may also be approached from below. To illustrate this concept, we have computed the reflected amplitude  $a_{\Gamma}^{+-}(x_{3e})$  and the incident amplitude  $a_{\Gamma}^{--}(x_{3e})$  in Fig. 5(a) and (b), under focal normalization. Since  $a_{\Gamma}^{--}(x_{3e}) = 1$  in this case, it follows that the reflected amplitude  $a_{\Gamma}^{+-}(x_{3e})$  is directly proportional to the reflectivity from below. In Fig. 5(c), we show the reflected amplitude  $a_{\Gamma}^{+-}(x_{3e})$  under physical normalization. Note that the reflectivity values have been overestimated in this case. To correct for this effect, we have to divide by the incident amplitude, which is shown in Fig. 5(d). In Fig. 5(e), we illustrate that this leads indeed to the reflectivity from below.

#### IV. IMAGING BY DOUBLE FOCUSING

As we have discussed in Section II-C, the Green's functions that we utilize for imaging are retrieved by applying focusing functions to the reflection response, which can be interpreted as single wavefield focusing (at the receiver side). Double

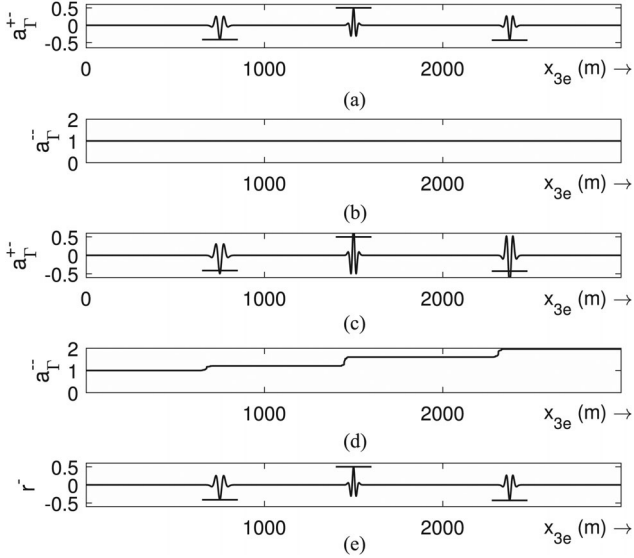


Fig. 5. Imaging by deconvolution from below. (a) Reflected amplitude  $a_{\Gamma}^{+-}(x_{3e})$  and (b) incident amplitude  $a_{\Gamma}^{-}(x_{3e})$  under focal normalization. (c) Reflected amplitude  $a_{\Gamma}^{+-}(x_{3e})$ , (d) incident amplitude  $a_{\Gamma}^{-}(x_{3e})$  and (e) their ratio (i.e. the reflectivity from below  $r^{-}(x_{3e})$ ) under physical normalization. The horizontal bars indicate the reflectivity values (computed directly from the model parameters) for reference.

wavefield focusing (at the source and the receiver side) can be realized by convolving the retrieved Green's functions with focusing functions again and summing over the acquisition surface. In Section IV-A and IV-B, we derive representations for double focusing (where reflectors are approached from above and from below, respectively). The imaging conditions are demonstrated with 1D synthetic examples in Section IV-C. In all cases, it is required that the Green's functions and focusing functions are correctly scaled, in order to extract quantitative information about the reflectivity. This requires physical normalization such that 13 is satisfied.

#### A. Approaching Reflectors From Above

We start with approaching the reflectors from above. To derive a representation for this scenario, we move the upper boundary of volume  $\mathcal{V}$  to the acquisition surface, i.e.  $\partial\mathcal{V}_i = \mathcal{S}_a$ , and we choose the lower boundary such that  $\mathbf{x}_p \in \partial\mathcal{V}_j$ , where  $\mathbf{x}_p$  is defined as a focal point. In state A, we introduce focusing function  $f_1^+(\mathbf{x}, \mathbf{x}_p)$ , which propagates in truncated medium 1, where truncation is applied at  $x_{3t} = x_{3p}$ . In state B, we place a source in the physical medium at  $\mathbf{x}_q$ , which can either be inside or outside  $\mathcal{V}$ , depending on the position of  $\mathbf{x}_p$ . This source radiates upwards in the upper mode and downwards in the lower mode. The constructed wavefields are given in Table IV, where source-receiver reciprocity relation 3 has been applied. By substituting these quantities in the reciprocity theorem of the convolution type 1, it can be derived that

$$G^{\pm+}(\mathbf{x}_q, \mathbf{x}_p) + \theta(x_{3p} - x_{3q}) f_1^{\pm}(\mathbf{x}_q, \mathbf{x}_p) = \int_{\mathcal{S}_a} G^{\pm+}(\mathbf{x}_q, \mathbf{x}) f_1^{\pm}(\mathbf{x}, \mathbf{x}_p) d^2\mathbf{x}. \quad (22)$$

TABLE IV  
WAVEFIELDS FOR IMAGING BY DOUBLE FOCUSING

| Field | State A                           | State B                                                                       |
|-------|-----------------------------------|-------------------------------------------------------------------------------|
| $p^+$ | $f_1^+(\mathbf{x}, \mathbf{x}_p)$ | $G^{+\mp}(\mathbf{x}, \mathbf{x}_q) = \pm G^{\pm-}(\mathbf{x}_q, \mathbf{x})$ |
| $p^-$ | $f_1^-(\mathbf{x}, \mathbf{x}_p)$ | $G^{-\mp}(\mathbf{x}, \mathbf{x}_q) = \mp G^{\pm+}(\mathbf{x}_q, \mathbf{x})$ |
| $s^+$ | 0                                 | $\chi^1 \delta(\mathbf{x} - \mathbf{x}_q)$                                    |
| $s^-$ | 0                                 | $\chi^0 \delta(\mathbf{x} - \mathbf{x}_q)$                                    |

Here,  $\theta(x_{3p} - x_{3q})$  is a Heaviside function, where  $\theta(x_{3p} - x_{3q}) = 0$  for  $x_{3p} < x_{3q}$  (in case  $x_{3q} \notin \mathcal{V}$ ),  $\theta(x_{3p} - x_{3q}) = \frac{1}{2}$  for  $x_{3p} = x_{3q}$  (in case  $x_{3q} \in \partial\mathcal{V}_j$ ) and  $\theta(x_{3p} - x_{3q}) = 1$  for  $x_{3p} > x_{3q}$  (in case  $x_{3q} \in \mathcal{V}$ ). When we choose  $\mathbf{x}_p = \mathbf{x}_q = \mathbf{x}_e$ , we can retrieve  $G^{-+}(\mathbf{x}_e, \mathbf{x}_e)$  by evaluating the right-hand side of 22 in the lower mode (note that  $f_1^-(\mathbf{x}_e, \mathbf{x}_e) = 0$ ). The reflectivity from above  $r^+(\mathbf{x}_e)$  can be extracted by integrating this quantity over frequency. Since deconvolution is not required, imaging by double focusing is expected to be relatively robust with respect to noise. Moreover, the solutions of the Marchenko equation  $G^{-+}$  and  $f_1^+$  that occur in the integrand can be expressed as a series which can be summed adaptively [26], [28]. This strategy seems especially fruitful in scenarios with poor signal-to-noise ratios.

#### B. Approaching Reflectors From Below

Reflectors may also be approached from below. To facilitate this strategy, we substitute the quantities in Table IV into the reciprocity theorem of the correlation type 2, yielding

$$G^{\pm-}(\mathbf{x}_q, \mathbf{x}_p) + \theta(x_{3p} - x_{3q}) f_1^{\mp*}(\mathbf{x}_q, \mathbf{x}_p) = \int_{\mathcal{S}_a} G^{\pm+}(\mathbf{x}_q, \mathbf{x}) f_1^{\mp*}(\mathbf{x}, \mathbf{x}_p) d^2\mathbf{x}. \quad (23)$$

If we evaluate this result in the upper mode just below the image point at  $\mathbf{x}_p = \mathbf{x}_q = \mathbf{x}_e^{+\epsilon}$ , we can retrieve  $G^{+-}(\mathbf{x}_e^{+\epsilon}, \mathbf{x}_e^{+\epsilon})$  (note that  $f_1^-(\mathbf{x}_e^{+\epsilon}, \mathbf{x}_e^{+\epsilon}) = 0$ ). The reflectivity from below  $r^-(\mathbf{x}_e)$  can be extracted by integrating  $\{\mathcal{E}(t^\epsilon, c(\mathbf{x}_e^{+\epsilon})) G^{+-}\}(\mathbf{x}_e^{+\epsilon}, \mathbf{x}_e^{+\epsilon})$  over frequency, where the extrapolation operator  $\mathcal{E}$  takes care of the two-way propagation path from  $\mathbf{x}_e^{+\epsilon}$  to  $\mathbf{x}_e$ .

#### C. Examples

We illustrate imaging by double focusing with a 1D synthetic experiment. We use the model and reflection data that were presented earlier in Fig. 3 and retrieve Green's functions and focusing functions under physical normalization. In Fig. 6(a) and (b), we show the reflectivity values  $r^+$  and  $r^-$  (where the reflectors are approached from above and from below, respectively). To obtain these results, we have evaluated the right-hand sides of 22 and 23. Note the close match with the reference reflectivity values, which are indicated in the figures.

## V. IMAGING BY CROSSCORRELATION

We may also retrieve the internal reflectivity by crosscorrelating Green's functions and summing over the acquisition surface

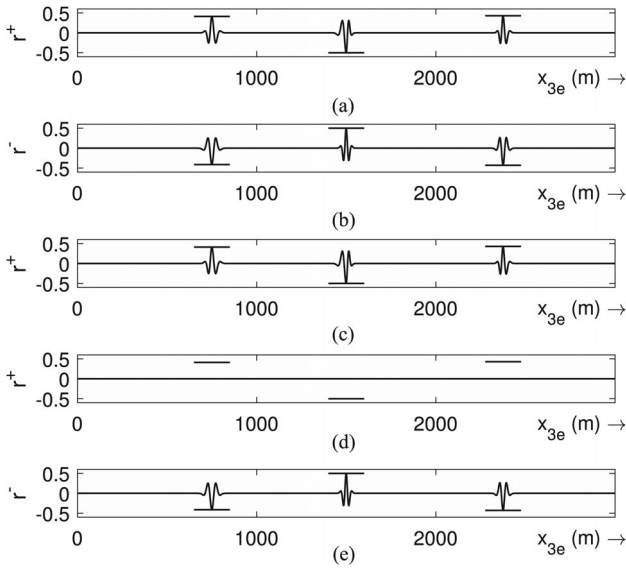


Fig. 6. Imaging by double focusing. Reflectivity from (a) above  $r^+(x_{3e})$  and (b) below  $r^-(x_{3e})$ . (c) Contributions of primary reflections to the image in (a) (to obtain this result, the right-hand side of 22 is evaluated with the first event in  $f_1^+(\mathbf{x}, \mathbf{x}_p)$  only). (d) Contributions of multiple reflections to the image in (a) (to obtain this result, the right-hand side of 22 is evaluated with the complete  $f_1^+(\mathbf{x}, \mathbf{x}_p)$  except its first event). (e) Contributions of primary reflections to the image in (b) (to obtain this result, the right-hand side of 23 is evaluated with the first event in  $G^{++}(\mathbf{x}_q, \mathbf{x})$  only). The horizontal bars indicate the reflectivity values (computed directly from the model parameters) for reference.

[24], [30], [31]. If this is done with single-sided illumination only, the retrieved amplitudes are inaccurate and not proportional to the actual internal reflectivity values. This strategy also results in crosstalk, which is caused by the crosscorrelation of different orders of reflections. Some remedies have been proposed to suppress the crosstalk [30]. Here, we show how an artifact-free result with accurate amplitudes can be obtained by using double-sided illumination rather than single-sided illumination. In Section V-A, we give a motivation for this imaging strategy. Then we derive a representation and a corresponding imaging condition in Section V-B. We illustrate the methodology with a synthetic 1D example in Section V-C and we offer some discussion on the utilization of multiple reflections in Section V-D.

#### A. Motivation

Given that a complete multi-source, multi-offset reflection response is acquired at a single acquisition boundary, the internal reflectivity can be accurately reconstructed, either by deconvolution or by double focusing. Based on causality arguments, it can be reasoned that the Green's functions contain no information before the direct wave, while focusing functions contain no information before the initial propagator [10]. As a consequence, the reflectivity values that are found by double focusing are derived from primary reflections only. To illustrate this statement, we recompute the image in Fig. 6(a) by evaluating the right-hand side of 22, where we use the first event of the downgoing focusing function  $f_1^+(\mathbf{x}, \mathbf{x}_p)$  only. This imaging condition has been demonstrated before for primary-based imaging [25], [26]. As illustrated in Fig. 6(c), the result of this procedure is similar

TABLE V  
WAVEFIELDS FOR IMAGING BY CROSSCORRELATION

| Field | State A                                                                       | State B                                                                          |
|-------|-------------------------------------------------------------------------------|----------------------------------------------------------------------------------|
| $p^+$ | $G^{+\mp}(\mathbf{x}, \mathbf{x}_p) = \pm G^{\pm-}(\mathbf{x}_p, \mathbf{x})$ | $G^{+\mp'}(\mathbf{x}, \mathbf{x}_q) = \pm' G^{\pm'-}(\mathbf{x}_q, \mathbf{x})$ |
| $p^-$ | $G^{-\mp}(\mathbf{x}, \mathbf{x}_p) = \mp G^{\pm+}(\mathbf{x}_p, \mathbf{x})$ | $G^{-\mp'}(\mathbf{x}, \mathbf{x}_q) = \mp' G^{\pm'+}(\mathbf{x}_q, \mathbf{x})$ |
| $s^+$ | $\chi^1 \delta(\mathbf{x} - \mathbf{x}_p)$                                    | $\chi^{0'} \delta(\mathbf{x} - \mathbf{x}_q)$                                    |
| $s^-$ | $\chi^0 \delta(\mathbf{x} - \mathbf{x}_p)$                                    | $\chi^{1'} \delta(\mathbf{x} - \mathbf{x}_q)$                                    |

to the result in Fig. 6(a). In Fig. 6(d), we confirm that the remaining events of  $f_1^+(\mathbf{x}, \mathbf{x}_p)$  do not contribute to the image. The same statement can be made when we approach the reflectors from below. In Fig. 6(e), we show that the reflectivity can be constructed with 23 even if we use the first event in  $G^{++}(\mathbf{x}_q, \mathbf{x})$  only. By similar reasoning, we can prove that also deconvolution-based images are constructed from primary reflections only [45].

In realistic scenarios, the acquired data is typically incomplete and contains additional noise. As a consequence, the images that are constructed by deconvolution or double focusing can be inaccurate [46]. It has been shown that internal multiple reflections contain additional information of the medium that can compensate for these inaccuracies [47]. One way to utilize these reflections is to use an imaging condition that is based on crosscorrelation rather than deconvolution or double focusing. This is the key idea behind so-called interferometric imaging [48], [49]. By crosscorrelating Green's functions, we can focus multiple reflections at the image points, such that they contribute physically to the image. Hence, in order to utilize the information that is contained in multiple reflections, we should replace the imaging condition by deconvolution or double focusing with an imaging condition that is based on crosscorrelation. In order to retrieve accurate reflectivity values without crosstalk, we should use double-sided illumination rather than single-sided illumination, as discussed before. Remember that double-sided illumination can be realized either by placing additional sources and receivers at  $\mathcal{S}_m$  or by retrieving virtual data at this surface.

#### B. Interferometric Imaging

To derive an imaging condition that is based on crosscorrelation, we let the boundaries of volume  $\mathcal{V}$  coincide with the acquisition surfaces, i.e.  $\partial\mathcal{V}_i = \mathcal{S}_a$  and  $\partial\mathcal{V}_j = \mathcal{S}_m$ . In state A, we place a source at  $\mathbf{x}_p$ , which radiates upwards in the upper mode and downwards in the lower mode. In state B, we place a source at  $\mathbf{x}_q$ , which radiates upwards in the upper' mode and downwards in the lower' mode. The constructed wavefields are shown in Table V. Next, we substitute these quantities into the reciprocity theorem of the correlation type 2, yielding

$$\begin{aligned}
& \pm G^{\pm\pm}(\mathbf{x}_q, \mathbf{x}_p) \pm' G^{\pm\pm'*}(\mathbf{x}_p, \mathbf{x}_q) \\
&= \int_{\mathcal{S}_a} G^{\pm+}(\mathbf{x}_q, \mathbf{x}) G^{\pm+*}(\mathbf{x}_p, \mathbf{x}) d^2\mathbf{x} \\
&+ \int_{\mathcal{S}_m} G^{\pm-}(\mathbf{x}_q, \mathbf{x}) G^{\pm-*}(\mathbf{x}_p, \mathbf{x}) d^2\mathbf{x}. \quad (24)
\end{aligned}$$

This result has been derived before in the context of seismic interferometry and has been used for Green's function retrieval between two receiver locations at  $\mathbf{x}_p$  and  $\mathbf{x}_q$  [50]. Hence, we refer to this type of imaging as interferometric imaging. The first integral on the right-hand side (evaluated in the upper-lower ' mode) has also been used for Marchenko imaging [24], [30], [31]. As we discussed earlier, this procedure leads to inaccurate amplitudes and artifacts. By using illumination at both acquisition boundaries  $\mathcal{S}_a$  and  $\mathcal{S}_m$ , an accurate image can be constructed without such artifacts. To approach the reflectors from above, we set  $\mathbf{x}_p = \mathbf{x}_q = \mathbf{x}_e^{-\epsilon}$  in the upper-lower ' mode, such that  $G^{-+}(\mathbf{x}_e^{-\epsilon}, \mathbf{x}_e^{-\epsilon}) - G^{+-*}(\mathbf{x}_e^{-\epsilon}, \mathbf{x}_e^{-\epsilon})$  can be retrieved. If we extrapolate this quantity to the image point with  $\mathcal{E}(t^\epsilon, c(\mathbf{x}_e^{-\epsilon}))$  and integrate over frequency, the reflectivity from above  $r^+(\mathbf{x}_e)$  can be extracted. We may also approach the reflectors from below by setting  $\mathbf{x}_p = \mathbf{x}_q = \mathbf{x}_e^{+\epsilon}$  in the lower-upper ' mode and following a similar procedure to extract the reflectivity from below  $r^-(\mathbf{x}_e)$ . Note that we can not retrieve the reflectivity properly by setting  $\mathbf{x}_p = \mathbf{x}_q = \mathbf{x}_e$ , due to (1) the finite-frequency limitations of the Marchenko equation and (2) the fact that the two Green's functions in the left-hand side of 24 are interfering.

### C. Examples

In this section, we demonstrate imaging by crosscorrelation with 1D synthetic examples, using the model and the reflection responses that were shown earlier in Fig. 3. We use the reflection data at both acquisition surfaces  $\mathcal{S}_a$  and  $\mathcal{S}_m$  to compute the relevant Green's functions and focusing functions by solving the Marchenko equation (under physical normalization). Then, we use 24 in the upper-lower ' mode in order to retrieve the reflectivity from above  $r^+$ . In Fig. 7(a), we show the contribution of the upper acquisition surface  $\mathcal{S}_a$ . Note that the reflectivity values of the deeper interfaces are underestimated in this case and that additional artifacts populate the image. In Fig. 7(b), we show the contribution of the lower acquisition surface  $\mathcal{S}_m$ . When this contribution is added to the image from  $\mathcal{S}_a$ , we achieve two objectives: (1) the underestimated amplitudes are corrected and (2) artifacts are removed. In Fig. 7(c), we demonstrate that this is indeed the case.

We have shown in the previous sections that the imaging conditions that are based on deconvolution or double focusing utilize information from primary reflections only. To illustrate that this is not the case for imaging by crosscorrelation, we differentiate the downgoing Green's function from the upper acquisition surface in a direct part and a coda. The same is done to the upgoing Green's function from the lower acquisition surface. Then, we recompute the image in Fig. 7(c) by using the direct parts of these Green's functions only. The result, which is shown in Fig. 7(d), can be interpreted as the contribution of primary reflections to the retrieved reflectivity values in Fig. 7(c). The contribution of multiple reflections follows by subtracting this result from Fig. 7(c), see Fig. 7(e). We can conclude from this figure that multiple reflections contribute physically to the retrieved reflectivity values of the deeper reflectors, which are under-illuminated by the primary reflections. This makes

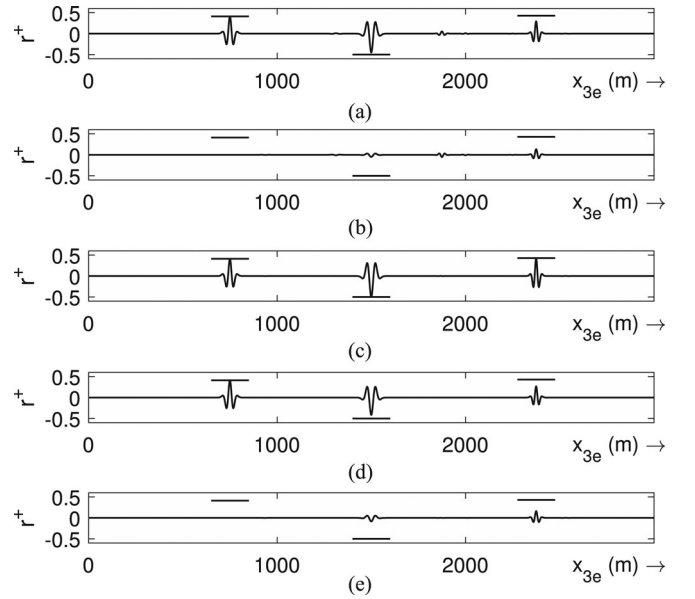


Fig. 7. Imaging by crosscorrelation. In (a) and (b) we show the contributions to the reflectivity from above  $r^+(x_{3e})$  from the acquisition surfaces  $\mathcal{S}_a$  and  $\mathcal{S}_m$ , respectively. The sum of (a) and (b) is given in (c). Contribution of (d) primary reflections and (e) multiple reflections to the image in (c). The horizontal bars indicate the reflectivity values (computed directly from the model parameters) for reference.

sense intuitively, since multiple reflections have been focused at the focal points.

### D. Discussion

Since (internal) multiple reflections can illuminate parts of the subsurface that are not illuminated by primary reflections, their utilization in the construction of images is an active topic of research in the seismic imaging community [46], [47]. Unfortunately, the Marchenko operator can only retrieve multiple reflections that illuminate an image point from a certain angle if this location is illuminated by the direct wave from the same angle [39]. Therefore, it is very unlikely that internal multiples which are retrieved by the multidimensional Marchenko equation can illuminate parts of the medium that are not illuminated by primary reflections. On the other hand, we have shown that the interferometric representation 24, which we used for imaging by crosscorrelation, allows us to propagate (internal) multiple reflections to the image points. We have also seen that double-sided illumination is required to meet this objective. As we indicated before, the reflection response at the lower acquisition surface  $\mathcal{S}_m$  can be computed from the reflection response at  $\mathcal{S}_a$  by inverting 18 at  $\partial\mathcal{V}_j = \mathcal{S}_m$ . It should be noticed that the information to construct the reflection response 'from below' by this procedure (including the multiple reflections) is derived mainly from the primary reflections in the data which are recorded from above [39]. However, the multiple reflections that are present in the upgoing wavefield  $G^{-+}(\mathbf{x}_q, \mathbf{x})$  in the first integral in 24 are physically recorded and they contribute to the retrieved reflectivity values when the proposed imaging condition is evaluated. For this reason, imaging by crosscorrelation might be beneficial to improve signal-to-noise ratios in strongly

heterogeneous media, where primary illumination may be weak and multiple reflections could provide secondary illumination.

## VI. PRACTICAL ISSUES

We finalize this paper with a discussion on some potential issues when Marchenko imaging is applied in practice. In Section VI-A, we focus on implementations in 2D and 3D, rather than 1D which was done in our examples. In Section VI-B, we elaborate on the sensitivity of Marchenko imaging to noise, where we point at several measures that have been proposed for improvement.

### A. Multidimensional Implementation

In this paper, we have demonstrated the proposed imaging conditions only in 1D synthetic media. For implementations in 2D media, we refer to the existing literature. Imaging by deconvolution has been demonstrated in e.g. [15], [22], [23]. To reduce the computational burden of this problem, it has recently been proposed to deconvolve the upgoing Green's function with the downgoing Green's function at a single focal point and stack over sources [31]. We emphasize that this approach is different from our proposal to image the upgoing and downgoing Green's functions independently and compute their ratio. The latter approach has yet to be demonstrated in 2D, but we expect results to be relatively accurate based on our previous experiences on related multidimensional problems [51]. Imaging by double focusing has been applied in 2D in [28]. However, physical normalization had not yet been implemented. For imaging by cross-correlation, 2D implementations can be found in [24], [30], [31]. Since illumination had been provided from one acquisition boundary only, artifacts emerged in all cases and the retrieved amplitudes were inaccurate. It is yet to be demonstrated in 2D and 3D that appropriate normalization and additional data from below leads to a superior image, as hypothesized in our current paper. In order to do so in practice, 13 needs to be satisfied (i.e. physical normalization should be enforced). In 1D, this could easily be achieved by inverting for an appropriate scalar at each focal point [41]. In 2D and 3D, an angle-dependent correction is likely to improve on this. Furthermore, it is not yet clear what would be the most efficient 2D implementation of extrapolation operator  $\mathcal{E}$ .

### B. Adaptive Implementation

Over the last few years, significant progress has been made in solving the multidimensional Marchenko equation for seismic field data. In order to improve robustness with respect to noise, it has been proposed to implement the methodology with adaptive filters [26]. This strategy has been successfully applied to field data in order to achieve imaging by double focusing [28]. An adaptive approach might also be relevant for imaging by crosscorrelation. Finally, we mention that robust results have also been reported by solving the Marchenko equation with a least-squares solver [52] or a sparse solver [53]. These approaches offer the flexibility to add regularization constraints for denoising purposes. Since the outcome of our imaging

conditions depends strongly on the quality of the retrieved Green's functions and focusing functions (which is not the topic of our current paper), we consider a further investigation on the impact of noise beyond our scope.

## VII. CONCLUSIONS

By solving the multidimensional Marchenko equation, one can retrieve focusing functions and Green's functions in an acoustic medium. We have defined two ways in which these wavefields can be normalized, which we refer to as focal normalization and physical normalization. We have distinguished three types of Marchenko imaging conditions: imaging by deconvolution, imaging by double focusing and imaging by cross-correlation.

For imaging by deconvolution, a substantial inverse problem is to be solved at each image point. The computational burden of this problem can be reduced significantly if we focus the reflected wavefield and the incident wavefield individually and compute their ratio. The procedure requires single-sided illumination only, where reflectors can be imaged either from above or from below. The procedure is independent on the normalization of the Green's functions and focusing functions that are derived from the Marchenko equation. It has been shown that internal multiples do not contribute to the construction of the image, when a deconvolution-based imaging condition is used.

Imaging by double focusing is computationally more straightforward than imaging by deconvolution or crosscorrelation. The methodology can be applied with single-sided illumination and reflectors can be approached either from above or from below. To retrieve accurate amplitudes, physical normalization should be enforced. Without such normalization, the method can still be applied to obtain artifact-free images, but the amplitudes of these images will be inaccurate. Akin to imaging by deconvolution, the information that is contained in internal multiple reflections is not utilized by this type of imaging condition. The double focusing methodology is relatively flexible and allows for adaptive implementation, which is not so straightforward when imaging is applied by deconvolution.

Artifact-free imaging by crosscorrelation requires illumination from two enclosing acquisition surfaces and can be used to approach reflectors from above or from below. Since multiple reflections are focused at the image points with this strategy, they contribute physically to the retrieved reflectivity, which may benefit imaging in weakly illuminated areas of strongly heterogeneous media, where primary illumination falls short. To implement this type of imaging in practice, it is crucial that physical normalization is enforced.

## REFERENCES

- [1] B. L. Biondi, *3D Seismic Imaging*. Tulsa, OK, USA: SEG, 2006.
- [2] P. N. T. Wells, "Ultrasonic imaging of the human body," *Rep. Prog. Phys.*, vol. 62, pp. 671–722, 1999.
- [3] J. F. Claerbout, *Fundamentals of Geophysical Data Processing*. Tulsa, OK, USA: Pennwell, 1985.
- [4] K. J. Langenberg, M. Berger, Th. Kreutter, K. Mayer, and V. Schmitz, "Synthetic aperture focusing technique signal processing," *NDT Int.*, vol. 19, no. 3, pp. 177–189, 1986.

- [5] M. F. Schiffrer and G. Schmitz, "Plane wave pulse-echo ultrasound diffraction tomography with a fixed linear transducer array," *Acoust. Imag.*, vol. 31, pp. 19–30, 2012.
- [6] K. P. Porter, "Diffraction-limited, scalar image formation with holograms of arbitrary shape," *J. Acoust. Soc. Amer.*, vol. 60, pp. 1051–1059, 1970.
- [7] M. L. Oristaglio, "An inverse scattering formula that uses all the data," *Inverse Probl.*, vol. 5, pp. 1097–1105, 1989.
- [8] A. Tarantola, *Inverse Problems Theory: Methods for Data Fitting and Model Parameter Estimation*. Amsterdam, The Netherlands: Elsevier, 1987.
- [9] K. Wapenaar, F. Broggini, E. Slob, and R. Snieder, "Three-dimensional single-sided Marchenko inverse scattering, data-driven focusing, Green's function retrieval, and their mutual relations," *Phys. Rev. Lett.*, vol. 110, no. 8, 2013, Art. no. 084301.
- [10] R. Burridge, "The Gel'fand-Levitan, the Marchenko and the Gopinath-Sondhi integral equations of inverse scattering theory, regarded in the context of inverse impulse-response problems," *Wave Motion*, vol. 2, no. 4, pp. 305–323, 1980.
- [11] J. H. Rose, "Single-sided autofocusing of sound in layered materials," *Inverse Probl.*, vol. 18, no. 6, pp. 1923–1934, 2002.
- [12] F. Broggini, R. Snieder, and K. Wapenaar, "Focusing the wavefield inside an unknown 1D medium: Beyond seismic interferometry," *Geophys.*, vol. 77, no. 5, pp. A25–A28, 2012.
- [13] Y. Zhang, N. Wang, and P. Wang, "One-dimensional single-sided acoustic focusing in a Goupillaud layered model," *J. Acoust. Soc. Amer.*, vol. 136, no. 5, pp. 2381–2388, 2014.
- [14] E. Slob, K. Wapenaar, F. Broggini, and R. Snieder, "Seismic reflector imaging using internal multiples with Marchenko-type equations," *Geophys.*, vol. 79, no. 2, pp. S63–S76, 2014.
- [15] K. Wapenaar, J. Thorbecke, J. van der Neut, F. Broggini, E. Slob, and R. Snieder, "Marchenko imaging," *Geophysics*, vol. 79, no. 3, pp. WA39–WA57, 2014.
- [16] A. E. Malcolm, M. V. de Hoop, and H. Calandra, "Identification of image artifacts from internal multiples," *Geophysics*, vol. 72, no. 2, pp. S123–S132, 2007.
- [17] G. F. Pinton, J. Dahl, and G. Trahlay, "Clutter and sources of image degradation in fundamental and harmonic ultrasound imaging," in *Proc. IEEE Int. Ultrason. Symp.*, 2009, vol. 18, pp. 2300–2303.
- [18] E. J. Alles, M. Jaeger, and J. C. Bamber, "Photoacoustic clutter reduction using short-lag spatial coherence weighted imaging," in *Proc. IEEE Int. Ultrason. Symp.*, 2014, vol. 23, pp. 41–44.
- [19] H.-M. Schwab, M. F. Beckmann, and G. Schmitz, "Photoacoustic clutter reduction by inversion of a linear scatter model using plane wave ultrasound measurements," *Biomed. Opt. Express*, vol. 7, no. 4, pp. 1468–1478, 2016.
- [20] M. J. A. Singh, M. Jaeger, M. Frenz, and W. Steenbergen, "In vivo demonstration of reflection artifact reduction in photoacoustic imaging using synthetic aperture photoacoustic-guided focused ultrasound (PAFUSion)," *Biomed. Opt. Express*, vol. 7, no. 8, pp. 2955–2972, 2016.
- [21] J. van der Neut, J. L. Johnson, K. van Wijk, S. Singh, E. Slob, and K. Wapenaar, "A Marchenko equation for acoustic inverse source problems," *J. Acoust. Soc. Amer.*, vol. 141, no. 6, pp. 4332–4346, 2017.
- [22] F. Broggini, R. Snieder, and K. Wapenaar, "Data-driven wave field focusing and imaging with multidimensional deconvolution: Numerical examples for reflection data with internal multiples," *Geophysics*, vol. 79, no. 3, pp. WA107–WA115, 2014.
- [23] X. Jia, A. Guitton, S. Singh, and R. Snieder, "Subsalt Marchenko imaging: A Gulf of Mexico example," in *Proc. Int. Meeting Soc. Exploration Geophys.*, 2017, pp. 5588–5592.
- [24] J. Behura, K. Wapenaar, and R. Snieder, "Autofocus imaging, Image reconstruction based on inverse scattering theory," *Geophysics*, vol. 79, no. 3, pp. A19–A26, 2014.
- [25] C. A. da Costa Filho, M. Ravasi, and A. Curtis, "Elastic P- and S-wave autofocus imaging with primaries and internal multiples," *Geophysics*, vol. 80, no. 5, pp. S187–S202, 2015.
- [26] J. van der Neut, K. Wapenaar, J. Thorbecke, E. Slob, and I. Vasconcelos, "An illustration of adaptive Marchenko imaging," *Leading Edge*, vol. 34, no. 7, pp. 818–822, 2015.
- [27] S. de Ridder, A. Curtis, J. van der Neut, and K. Wapenaar, "Marchenko wavefield redatuming, imaging conditions, and the effect of model errors," in *Proc. Int. Meeting Soc. Exploration Geophys.*, 2016, pp. 5155–5159.
- [28] M. Staring, R. Pereira, H. Douma, J. van der Neut, and K. Wapenaar, "Adaptive double-focusing method for source-receiver Marchenko redatuming on field data," in *Proc. Int. Meeting Soc. Exploration Geophys.*, 2017, pp. 4808–4812.
- [29] C. A. da Costa Filho, G. A. Meles, A. Curtis, M. Ravasi, and A. Kritski, "Imaging strategies using Marchenko focusing functions," in *Proc. EAGE Conf. Exhib.*, 2017, Paper P915.
- [30] C. A. da Costa Filho and A. Curtis, "Attenuating multiple-related imaging artifacts using combined imaging conditions," *Geophysics*, vol. 81, no. 6, pp. S469–S475, 2016.
- [31] S. Singh and R. Snieder, "Strategies for imaging with Marchenko-retrieved Green's functions," *Geophysics*, vol. 82, no. 4, pp. Q23–Q37, 2017.
- [32] C. P. A. Wapenaar and J. L. T. Grimbergen, "Discrete time solution of plane P-SV waves in a plane layered medium," *Geophysics*, vol. 35, pp. 197–219, 1970.
- [33] M. V. de Hoop, "Generalization of the Bremmer coupling series," *J. Math. Phys.*, vol. 37, pp. 3246–3282, 1996.
- [34] C. P. A. Wapenaar and J. L. T. Grimbergen, "Reciprocity theorems for one-way wave fields," *Geophys. J. Int.*, vol. 127, no. 1, pp. 169–177, 1996.
- [35] A. T. de Hoop, *Handbook of Radiation and Scattering of Waves*. London, U.K.: Academic, 1995.
- [36] K. Wapenaar, J. van der Neut, and E. Slob, "Unified double- and single-sided homogeneous Green's function representation," *Proc. Roy. Soc. Amer.*, vol. 474, Art. no. 02160162, 2016.
- [37] I. Vasconcelos and J. Rickett, "Broadband extended images by joint inversion of multiple blended wavefields," *Geophysics*, vol. 78, no. 2, pp. WA147–WA158, 2013.
- [38] C. Mildner, F. Broggini, J. O. A. Robertsson, D.-J. van Manen, and S. Greenhalgh, "Target-oriented velocity analysis with Marchenko redatumed data," *Geophysics*, vol. 82, no. 2, pp. R75–R86, 2017.
- [39] J. van der Neut, I. Vasconcelos, and K. Wapenaar, "On Green's function retrieval by iterative substitution of the coupled Marchenko equations," *Geophys. J. Int.*, vol. 203, no. 2, pp. 792–813, 2015.
- [40] A. J. Berkhou, *Seismic Migration: Imaging of Acoustic Energy by Wave Field Extrapolation*. Amsterdam, The Netherlands: Elsevier, 1984.
- [41] J. Brackenhoff, "Rescaling of incorrect source strength using Marchenko redatuming," M.Sc. dissertation, Dept. Geosci. Eng., Delft Univ. Tech., Delft, The Netherlands, 2016.
- [42] C. G. M. de Bruin, C. P. A. Wapenaar, and A. J. Berkhou, "Angle-dependent reflectivity by means of prestack migration," *Geophysics*, vol. 55, no. 9, pp. 1223–1234, 1990.
- [43] K. Aki and P. G. Richards, *Quantitative Seismology*, 2nd ed., Sausalito, CA, USA: Univ. Sci. Books, 1980.
- [44] Y. Wang, "Frequencies of the Ricker wavelet," *Geophysics*, vol. 80, no. 2, pp. A31–A37, 2015.
- [45] K. Wapenaar, J. van der Neut, and E. Slob, "On the role of multiples in Marchenko imaging," *Geophysics*, vol. 82, no. 1, pp. A1–A5, 2017.
- [46] A. J. Berkhou, "Utilization of multiple scattering: The next big step forward in seismic imaging," *Geophys. Prospecting*, vol. 65, no. 1, pp. 106–145, 2017.
- [47] M. Davydenko and D. J. Verschuur, "Full-wavefield migration - using surface and internal multiples in imaging," *Geophys. Prospecting*, vol. 65, no. 1, pp. 7–21, 2017.
- [48] I. Vasconcelos, R. Snieder, and B. Hornby, "Imaging internal multiples from subsalt VSP data - Examples of target-oriented interferometry," *Geophysics*, vol. 73, no. 4, pp. S157–S168, 2008.
- [49] G. T. Schuster, *Seismic Interferometry*. Cambridge U.K.: Cambridge Univ. Press, 2009.
- [50] K. Mehta, A. Bakulin, J. Sheiman, R. Calvert, and R. Snieder, "Improving the virtual source method by wavefield separation," *Geophysics*, vol. 72, no. 4, pp. V79–V86, 2007.
- [51] J. van der Neut, "Downhole interferometric illumination diagnosis and balancing," *Geophys. Prospecting*, vol. 61, no. 1, pp. 352–367, 2013.
- [52] M. Ravasi, "Rayleigh-Marchenko redatuming for target-oriented, true-amplitude imaging," *Geophysics*, vol. 82, no. 6, pp. S439–S452, 2017.
- [53] M. Staring, J. van der Neut, N. Grobbe, and K. Wapenaar, "Sparse inversion for solving the coupled Marchenko equations including free-surface multiples," in *Proc. EAGE Conf. Exhib.*, 2017, Paper P914.